Journal of The Electrochemical Society, 2022 **169** 100550
1945-7111/2022/169(10)/100550/10/$40.00 © 2022 The Electrochemical Society ("ECS"). Published on behalf of ECS by IOP Publishing Limited

Impact of Carbon Binder Domain on the Performance of Lithium-metal Batteries

Francesca Boso,[1] Weiyu Li,[1] Kimoon Um,[2] and Daniel M. Tartakovsky[1,z]

[1]*Department of Energy Science and Engineering, Stanford University, Stanford, California 94305, United States of America*
[2]*Research & Development Division, Hyundai Motor Group, Gyeonggi-do, 16082, Republic of Korea*

Pseudo-2-dimensional models are routinely used to predict the lithiation curves for energy storage devices, including lithium-metal batteries. The performance of such models is as good as their parameterization, which remains a challenge especially in the presence of carbon binder domain (CBD). We propose two alternative parameterization strategies, which explicitly account for the CBD volume fraction and physical properties. The first aggregates CBD with the electrolyte-filled pore space and expresses the Bruggeman exponent in terms of a solution of microstructure-specific closure problem. The second treats CBD and active particles as a composite solid phase, whose effective properties are computed (semi-)analytically via homogenization. We show that the latter strategy used to parameterize the Doyle-Fuller-Newman model provides an attractive middle ground between the model complexity and the prediction accuracy. Our modeling results suggest that the battery discharge time decreases as either the CBD volume fraction increases or the CBD ionic diffusivity decreases, and is insensitive to the CBD ionic conductivity. The quantitative nature of these observations can be used in the optimal design of porous cathodes.
 [DOI: 10.1149/1945-7111/ac9a82]

Manuscript submitted July 23, 2022; revised manuscript received September 13, 2022. Published October 31, 2022.

Porous materials play a central role in energy storage devices such as lithium-based batteries. For example, the cathodes of both Li-ion and Li-metal batteries are typically composed of active porous materials (transition-metal oxide particles),[1] the anode of a Li-ion battery is made of porous graphite,[2] and a porous separator is placed between the two electrodes. Pore-scale material properties, e.g., the size and spatial arrangement of (transition-metal oxide) active material particles in an electrode[3] or the columnized structure of a separator,[4] can be used to optimize the performance of a device. That is because such pore-scale characteristics control device-scale transport of lithium ions, Li^+, and, ultimately, battery performance and aging.

Among other relevant pore-scale quantities, the so-called carbon binder domain (CBD)[5,6] is ubiquitous yet least studied. CBD refers to the mixed phase comprising carbon additives (e.g., carbon black) and a binder, which surrounds active particles. It is routinely used to improve the electric conductivity and mechanical stability of porous electrodes.[6,7] Despite its benefits, CBD hinders the intercalation of Li^+ from the electrolyte to the active particles by increasing the tortuosity of diffusion pathways and reducing the active surface area, thus leading to performance reduction, especially at high current.[8–10] Pore-scale heterogeneity of CBD distribution also impacts a device's overall performance.[11]

Complexity of the fabrication process and challenges in tomographic imagining of composite materials prevent the accurate characterization of the microstructure of porous electrodes, undermining the ability to distinguish between different solid phases and between the solid phase and the pore space. In particular, it is often difficult to distinguish between the pore space and CBD, which is virtually invisible in tomographic scans.[12] Yet, this information is needed for pore-scale numerical simulations of Li-metal batteries. That is why, despite advances in imaging techniques,[13] pore-scale electrochemical simulations often rely on synthetically-enhanced realizations of the porous structure, which supplement the topology of the active material from imaging with synthetic CBD configurations.[12,14–16] The latter process relies on morphological hypotheses about CBD distribution, e.g., assuming that active particles are covered with a uniform CBD coat or prescribing irregular CBD structures to reflect the possible tendency of CBD deposition to adhere to itself rather than to an active material surface.[12,17]

Continuum-scale simulations of physicochemical processes in porous media both obviate the need for this elusive information and significantly accelerate the computation by averaging out the pore-scale variability and replacing various phases of an electrolyte-filled porous material with a single continuum characterized by aggregate properties such as porosity and tortuosity.[18,19] The pseudo-two-dimensional (P2D) models[20,21] occupy the middle ground between these pore- and continuum-scale simulation frameworks in that they retain a micro-scale description of transport in the active solid-phase but represent the latter as an effective/equivalent sphere or a collection of spheres. Like all effective/continuum-scale models, the P2D models and their various simplifications[22] trade the high-fidelity of pore-scale simulations for computational efficiency.

Current implementations of the P2D models lump the CBD phase with the electrolyte-filled pore space and rely on empirical corrections of the tortuosity coefficient to account for the presence of CBD.[13,23] In this setting, automated techniques[24] can be used to estimate tortuosity from tomographic data; and its CBD-related corrections can be constructed to account for, e.g., the overall porosity, the physics of CBD deposition during fabrication, and the active particles' geometry.[23] This procedure relies on pore-scale simulations of solute transport in a representative elementary volume of the imaged porous material and, crucially, ignores transport properties (e.g., ionic diffusion coefficient and ionic conductivity) of the CBD phase.

To explicitly account for the physicochemical characteristics of the CBD phase, we propose a parameterization of the P2D models that treats the two solid phases (active material and CBD) as a single homogenized solid phase. That is in contrast to the current approaches[13,23] that aggregate the solid (CBD) and fluid (electrolyte) phases into an equivalent liquid phase. Our parameterization utilizes the homogenization results[25] for a CBD/active-material spherical composite, which are based on mass and charge conservation in the presence of ion intercalation into an active particle coated by CBD. The equivalent properties of this solid composite are expressed in terms of the CBD volume fraction and transport properties of the active material and CBD. Our parameterization strategy offers three practical benefits. First, by relying on the readily available volume fraction rather than pore-scale topology, it does not confront the above-mentioned limitations of electrode imaging; the latter serve as raison d'être for the less intuitive parameterization strategies currently in use. Second, our approach is significantly more computationally efficient than its alternatives,[13,23] because it yields a (semi-)analytical parameterization without resorting to pore-scale simulations that underpin the latter. Third, the dependence of our results on the CBD volume fraction and properties of CBD and active material facilitates the optimal design of battery electrodes.

[z]E-mail: tartakovsky@stanford.edu

We compare the performance of the two alternative parameterizations of widely used P2D models—the Doyle-Fuller-Newman (DFN) model[20] and the multi-particle DFN (mDFN) model[21]—and of their simplified version encapsulated in the single-particle model[26] (SPM). In this comparison, the predictions of lithiation curves derived from the pore-scale simulations of a porous cathode with given CBD morphology[12] serve as "ground truth".[a] Our numerical experiments reveal the superior performance of the DFN model with our parameterization. This model's sensitivity to variations in CBD properties and ease of use make it a viable tool for prediction and design.

Continuum-Scale Models

P2D models of a Li-metal battery describe the spatial variability of Li^+ concentration and electric potential in the through-cell (x) direction, neglecting their variability in the transverse direction. Let us place the inner surface of a Li-metal anode at $x = 0$, so that a separator of length L_{sep} occupies the interval $0 < x < L_{sep}$ and a porous cathode of length L_{cat} lies in the interval $L_{sep} \leqslant x \leqslant L$, where $L = L_{cat} + L_{sep}$. Then the device-scale spatiotemporal evolution of the Li^+ concentration, $c^e(x, t)$, and electric potential, $\phi^e(x, t)$, in the electrolyte satisfy the one-dimensional partial-differential equations (PDEs)

$$\frac{\partial \omega c^e}{\partial t} = \frac{\partial}{\partial x}\left(D^e_{eff}\frac{\partial c^e}{\partial x}\right) + A_{rs}\frac{1-t^+}{F}j, \qquad 0 < x < L, \quad t > 0 \tag{1a}$$

and

$$\frac{\partial}{\partial x}\left(K^e_{eff}\frac{\partial \varphi^e}{\partial x} + \kappa^s_{eff}\frac{\partial \ln c^e}{\partial x}\right) + A_{rs}j = 0, \qquad 0 < x < L, \quad t > 0. \tag{1b}$$

Here, $\omega(x)$ is the porosity of the separator and cathode; D^e_{eff} and K^e_{eff} are, respectively, the effective ionic diffusion coefficient and effective ionic conductivity of the electrolyte in the presence of the porous material; $A_{rs}(x)$ is the specific reactive surface of the cathode, i.e., $A_{rs} = 0$ for $0 < x < L_{sep}$; $j(x, t)$ is the current density, with $j = 0$ for $0 < x < L_{sep}$; and the lumped parameter $\kappa^s_{eff} = 2RTK^e_{eff}(t^+ - 1)\lambda/F$ is expressed in terms of the effective ionic conductivity K^e_{eff}, the temperature T, the cation transference number t^+ (a given function of c^e), the activity coefficient λ, and the gas (R) and Faraday (F) constants. The P2D models also track the spatiotemporal evolution of Li^+ concentration, c^s, and electric potential, ϕ^s, within the solid phase (active material) of the porous electrode. In so doing, the solid phase with complex microstructure is replaced by a collection of non-overlapping spheres of either identical radius R^s or various radii.[b] In the former case, i.e., in the DFN model, the specific reactive surface A_{rs} acquires a simple expression $A_{rs} = 3(1-\omega)/R^s$; and the Li^+ concentration, $c^s(r, t; x)$, and electric potential, $\phi^s(r, t; x)$, vary in the radial (r) direction within the sphere according to

$$\frac{\partial c^s}{\partial t} = \frac{1}{r^2}\frac{\partial}{\partial r}\left(D^s r^2 \frac{\partial c^s}{\partial r}\right), \qquad 0 < r < R^s, \quad t > 0, \tag{1c}$$

$$\sigma^s_{eff}\frac{\partial^2 \varphi^s}{\partial x^2} = A_{rs}j, \qquad L_{sep} < x < L, \quad t > 0, \tag{1d}$$

where D^s is the diffusion coefficient for Li^+ in the solid phase and σ^s_{eff} is the effective conductivity of the solid phase in the porous cathode. Processes in the electrolyte phase (Eqs. 1a and 1b) and the solid phase (Eqs. 1c and 1d) are coupled due to ion intercalation at the solid/liquid interface. In the DFN model, this interface is the surface of each solid sphere, $r = R^s$. Specifically, under certain conditions, the Butler-Volmer equation,

$$j = 2Fk_0\sqrt{c^e(x, t)c^s(R^s, t; x)}\sqrt{c^s_{max} - c^s(R^s, t; x)}\sinh\left(\frac{F\eta}{2RT}\right), \qquad L_{sep} \leqslant x \leqslant L, \tag{1e}$$

relates the current density $j(x, t)$ in Eqs. 1a–1d to the Li^+ concentrations and electric potentials both in the electrolyte, $c^e(x, t)$ and $\phi^e(x, t)$, and on the active material's surface, $c^s(R^s, t; x)$ and $\phi^s(R^s, t; x)$. In this relation, k_0 is the reaction rate constant; c^s_{max} is the maximum concentration in the solid phase; $\eta(x, t) = \phi^s(R^s, t; x) - \phi^e(x, t) - U_{ocp}$ is the cell overpotential; and the open circuit potential U_{ocp} is a given function of $c^s(R^s, t; x)/c^s_{max}$. In the mDFN model, $j(x, t)$ is averaged over the particle size distribution.

SPM represents a reduced-complexity counterpart of the DFN model, which neglects mass transport in the electrolyte. Instead of solving Eq. 1a, SPM assumes the Li^+ concentration in the electrolyte, c^e, to be uniform.

Equations 1 are subject to initial and boundary conditions, which reflect a battery's operating regime. To be concrete, we consider a battery with spatially uniform Li^+ concentrations in the electrolyte and the solid phase, c^e_{in} and c^s_{in}, which gives rise to the initial conditions

$$c^e(x, 0) = c^e_{in}, \quad 0 < x < L; \qquad c^s(r, 0) = c^s_{in}, \quad 0 < r < R^s. \tag{2a}$$

To simulate a battery discharging with the constant discharge current density i_{dis}, we impose the boundary conditions

$$-D^e_{eff}\frac{\partial c^e}{\partial x}(0, t) = \frac{1-t_+}{F}i_{dis}, \qquad \frac{\partial c^e}{\partial x}(L, t) = 0, \qquad t > 0; \tag{2b}$$

$$-K^e_{eff}\frac{\partial \varphi^e}{\partial x}(0, t) - \kappa^e_{eff}\frac{\partial \ln c^e}{\partial x}(0, t) = i_{dis}, \qquad t > 0; \tag{2c}$$

$$K^e_{eff}\frac{\partial \varphi^e}{\partial x}(L, t) + \kappa^e_{eff}\frac{\partial \ln c^e}{\partial x}(L, t) = 0, \qquad t > 0; \tag{2d}$$

$$\frac{\partial \varphi^s}{\partial x}(L_{sep}, t) = 0, \qquad -\sigma^s_{eff}\frac{\partial \varphi^s}{\partial x}(L, t) = i_{dis}, \qquad t > 0. \tag{2e}$$

This formulation automatically satisfies the continuity conditions at the separator/electrode interface, $x = L_{sep}$. Finally, the boundary conditions for the solid particles are

$$\frac{\partial c^s}{\partial r}(0, t; x) = 0, \qquad -D^s\frac{\partial c^s}{\partial r}(R^s, t; x) = \frac{j(x, t)}{F}, \qquad t > 0, \qquad L_{sep} \leqslant x \leqslant L. \tag{2f}$$

Alternative parameterizations of P2D models.—The effective parameters D^e_{eff}, K^e_{eff}, and σ^s_{eff} in the P2D models can be related to their counterparts in the corresponding free phase (the diffusion

[a] The failure of P2D models to predict experimental lithiation curves at high C-rates has at least two sources: the errors in material characterization and the questionable validity of multiple approximations that underpin the upscaling (homogenization) of the underlying pore-scale models. We focus on the former source of prediction error by treating the pore-scale simulations as exact, even when their predictions of lithiation curves differ from observations[12] due to errors in material characterization and representation.

[b] The former approach, the DFN model, implicitly assumes the cathode microstructure to be uniform; the latter, the mDFN model,[21] aims to capture heterogeneity of the cathode's microstructure.

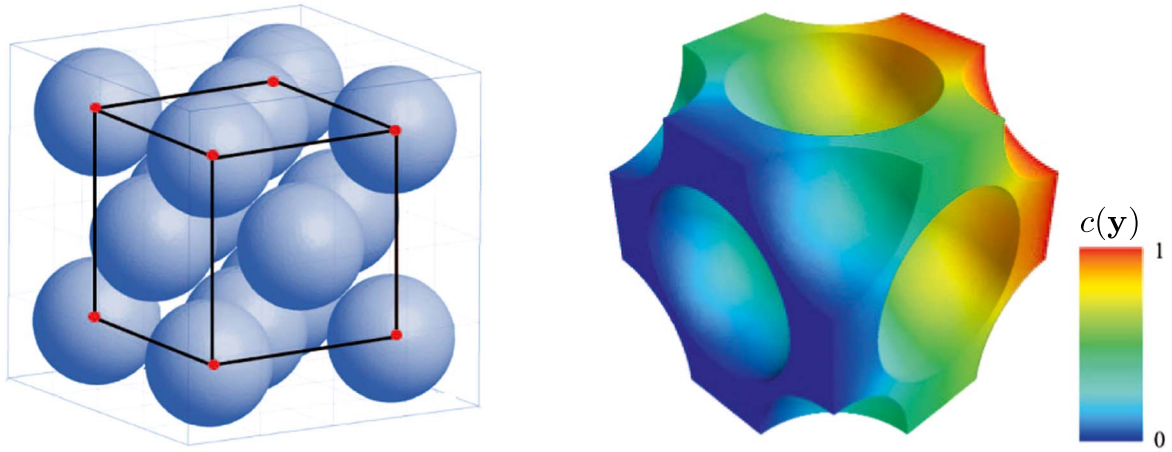

Figure 1. Face-Centered-Cubic arrangement of the active-material particles (Left) and a representative solution, $c(\mathbf{y})$, to the closure problem in Eq. 4 (Right), which is used to calculate the Bruggeman exponent b^{e}. This solution corresponds to $c_{\mathrm{L}} = 0$ and $c_{\mathrm{R}} = 1$.

coefficients of Li^+ in a given electrolyte, D^{e}; and the ionic conductivities of the electrolyte and the solid phase, K^{e} and σ^{s}) and the microstructure of the porous material via homogenization.[18,27] In lieu of such procedures, which can be computationally demanding, it is common to deploy the Bruggeman relations,[18,23,27]

$$D^{\mathrm{e}}_{\mathrm{eff}} = \omega^{b^{\mathrm{e}}} D^{\mathrm{e}}, \qquad K^{\mathrm{e}}_{\mathrm{eff}} = \omega^{b^{\mathrm{e}}} K^{\mathrm{e}}, \qquad \sigma^{\mathrm{s}}_{\mathrm{eff}} = (1-\omega)^{b^{\mathrm{s}}} \sigma^{\mathrm{s}}, \qquad [3]$$

where b^{e} and b^{s} are the Bruggeman exponents, which are often set to 1.5.[c]

We consider two alternative strategies for incorporation of CBD into this parameterization of the P2D models. The currently used approach is to lump together the electrolyte and CBD phases;[13,23] consequently, we refer to it as the augmented electrolyte (AE) parameterization. Our approach is to aggregate the two solid phases, the active material and CBD, instead; we refer to it as the augmented material (AM) parameterization. Our implementation of both strategies is detailed below.

AE parameterization. Combining the CBD phase with the electrolyte-filled pores modifies the actual porosity of the cathode, ω. If the volume fraction of the active material in the solid phase is v, then the resulting "lumped" porosity is $\varepsilon = \omega + (1-\omega)(1-v)$ and the volume fraction of the active material (the only remaining solid phase) is $1-\varepsilon$. The simplest version of the AE parameterization of the P2D models modifies the Bruggeman Eqs. 3 by replacing ω with ε, leaving the remaining properties unchanged. This procedure ignores the physicochemical characteristics of CBD, but can be enhanced to account for some of this information.[13,23]

We also test a more elaborate way to compute the Bruggeman exponent b^{e} in Eq. 3, which relies on pore-scale simulations of transport of a chemically inert solute in a representative elementary volume (REV) of the porous cathode.[24] The REV Ω_{REV} of a three-dimensional porous material is a cube of length L_{REV} that is composed of the fluid phase (the electrolyte-filled pores) Ω_{e} and the solid phase Ω_{s}, i.e., $\Omega_{\mathrm{REV}} = \Omega_{\mathrm{e}} \cup \Omega_{\mathrm{s}}$. In the AM parameterization, the "pore space" $\Omega = \Omega_{\mathrm{e}} \cup \Omega_{\mathrm{CBD}}$ comprises the electrolyte phase Ω_{e} and CBD Ω_{CBD}, while the solid phase is reduced to the active material domain Ω_{am}, such that $\Omega_{\mathrm{REV}} = \Omega \cup \Omega_{\mathrm{am}}$. The spatial distribution of the solute concentration, $c(\mathbf{y})$, within the pore space Ω is described by the three-dimensional PDE

$$\nabla\cdot(D(\mathbf{y})\nabla c) = 0, \qquad \mathbf{y} \in \Omega, \qquad [4a]$$

that is subject to the boundary conditions along the surface $\partial\Omega$ bounding the pore space Ω,

$$c(\mathbf{y} \in \partial\Omega_{\mathrm{L}}) = c_{\mathrm{L}}; \qquad c(\mathbf{y} \in \partial\Omega_{\mathrm{R}}) = c_{\mathrm{R}};$$
$$\nabla c\cdot\mathbf{n} = 0, \quad \mathbf{y} \in \partial\Omega/(\partial\Omega_{\mathrm{L}} \cup \partial\Omega_{\mathrm{R}}). \qquad [4b]$$

The mass flux, $-D\nabla c$, is driven by the difference between the concentrations c_{L} and c_{R} imposed at the two opposite (Left and Right) faces of the REV, $\partial\Omega_{\mathrm{L}}$ and $\partial\Omega_{\mathrm{R}}$, whereas no-flux boundary conditions are assigned to all other boundaries, identified by the outward unit vector $\mathbf{n}$. The tortuosity factor and, hence, the corresponding Bruggeman exponent b^{e} are computed by equating the overall flux crossing the REV and the equivalent homogeneous cube.

While one could use tomographic images to estimate $\partial\Omega$,[15,23] for our purpose it is sufficient to consider a porous cathode consisting of identical spheres arranged into a Face-Centered-Cubic lattice (Fig. 1); the radius of these spheres is selected to achieve the prescribed porosity ε. Unlike the previous studies of this kind, we explicitly account for the diffusive coefficient of CBD, D^{CBD}, by letting the diffusion coefficient $D(\mathbf{y})$ to vary in space:

$$D(\mathbf{y}) = \begin{cases} D^{\mathrm{e}} & \mathbf{y} \in \Omega_{\mathrm{e}} \\ D^{\mathrm{CBD}} & \mathbf{y} \in \Omega_{\mathrm{CBD}}. \end{cases}$$

The closure problem in Eq. 4 is solved once, at the beginning of the simulations, to compute the Bruggeman exponent b^{e}. A representative solution of the closure problem is shown in Fig. 1.

AM parameterization. This new strategy leaves the electrolyte-filled pore space, Ω_{e}, untouched, while accounting for the composite nature of the solid phase, $\Omega_{\mathrm{s}} = \Omega_{\mathrm{am}} \cup \Omega_{\mathrm{CBD}}$. A porous cathode is assumed to consist of active spherical particles of radius R_{am}, which are coated with a CBD layer of thickness d_{CBD}, such that the volume fraction of active material in the solid phase is $v = R^2_{\mathrm{am}}/(R_{\mathrm{am}} + d_{\mathrm{CBD}})^2$. The effective (homogenized) physicochemical properties of the solid particle of radius $\tilde{R}^{\mathrm{s}} = R_{\mathrm{am}} + d_{\mathrm{CBD}}$ are[25]

$$\tilde{D}^{\mathrm{s}} = \left[\frac{v^{2/3}}{D^{\mathrm{s}}} + 5\frac{1-v}{D^{\mathrm{CBD}}}\left(\frac{(1-v^{1/3})^2 + 3(v^{1/3}+2)(1-v^{1/3})}{2(1-v^{1/3})^2 + 6v^{1/3}} - \frac{3(1-v^{1/3})^2}{1-v}\right)\right]^{-1}, \qquad [5a]$$

[c]We choose the Bruggeman relations because of their widespread use in battery simulations, even though more accurate and robust representations are available.[18,19] This choice is sufficient to demonstrate how our approach allows one to incorporate CBD into existing models, which might or might not rely on the Bruggeman relations.

Table I. Geometric and electrochemical parameters used both in our analysis and to construct the reference lithiation curves.[12,16] The functional dependencies are given in Section 4 of Ref. 16.

Porous electrode		
Initial Li concentration [mol/m^3]	$c^{\mathrm{s}}_{\mathrm{in}}$	18 409.57
Maximum Li concentration [mol/m^3]	$c^{\mathrm{s}}_{\mathrm{max}}$	50 451
NCM ionic conductivity [S/m]	σ^{s}	2.8
CBD ionic conductivity [S/m]	σ^{CBD}	0.0169
NCM ionic diffusivity [m^2/s]	D^{s}	$4.3032 \cdot 10^{-14}$
CBD ionic diffusivity [m^2/s]	D^{CBD}	$7.6597 \cdot 10^{-16}$
Reaction rate constant [m$^{2.5}$/s/mol$^{0.5}$]	k_0	$1.5228 \cdot 10^{-11}$
Open circuit potential [V]	U_{ocp}	function of $c^{\mathrm{s}}/c^{\mathrm{s}}_{\mathrm{max}}$
Cathode thickness [μm]	L_{cat}	59
Active material volume fraction in the REV [−]	$1-\varepsilon$	0.583
CBD volume fraction in the REV [−]	$(1-\omega)(1-v)$	0.112
Active particle representative radius [μm]	R^{s}	7.84
Coefficient of variation of R^{s} [−]	σ_r/R^{s}	0.46
Electrolyte (values at $c^{\mathrm{e}}_{\mathrm{in}}$)		
Initial Li^+ concentration [mol/m]	$c^{\mathrm{e}}_{\mathrm{in}}$	1000
Ionic conductivity for Li^+ [S/m]	K^{e}	0.95; function of c^{e}
Transference number [−]	t^+	0.2527; function of c^{e}
Diffusivity [m^2/s]	D^{e}	$3.7621 \cdot 10^{-10}$; function of c^{e}
Activity term [−]	λ	1.9865; function of c^{e}
Separator		
Thickness [μm]	L_{sep}	100
Porosity [−]	ω_{sep}	0.5
Cell characteristics & operating conditions		
Nominal cell capacity [mAh]	Q_{nom}	3.6192
Cell area [cm^2]	A	1.131
Applied current density [mA/cm^2]	i_{dis}	{1, 3, 6, 12}
Temperature [K]	T	298.15
Lower voltage cutoff [V]	V_{low}	3.0
Upper voltage cutoff [V]	V_{up}	4.2

$$\tilde{\sigma}^{\mathrm{s}} = \frac{2\sigma^{\mathrm{s}}\sigma^{\mathrm{CBD}}}{\frac{\sigma^{\mathrm{s}}(v^{-1/3}-1)}{1-v^{1/3}(v^{1/3}+1)^2} + 2\sigma^{\mathrm{CBD}}v^{-1/3}},$$

$$\tilde{k}_0 = k_0 v^{6/7}\sqrt{\frac{1+2v^{1/3}}{7+2v^{1/3}}}, \qquad \tilde{c}^{\mathrm{s}}_{\mathrm{max}} = c^{\mathrm{s}}_{\mathrm{max}}\, v, \qquad [5b]$$

$$\tilde{c}^{s}_{\mathrm{in}} = c^{s}_{\mathrm{in}} v + c^{e}_{\mathrm{in}}(1-v). \qquad [5c]$$

These expressions are derived by ensuring that the mass and charge entering the composite particle are the same as those entering the homogenized particle. They are strictly valid for operating conditions under which the intercalation delay time $t_{\mathrm{del}} = d^2_{\mathrm{CBD}}/D^{\mathrm{CBD}}$ is negligible. Otherwise, the constant homogenized parameters in Eq. 5 should be replaced with their time-dependent counterparts;[25] we refer to the approach that replaces the constant $\tilde{D}^{\mathrm{s}}$ with $\tilde{D}^{\mathrm{s}}(t)$ as the AM+ parameterization.

The AM parameterization of the P2D models, Eqs. 1–3, consists of replacing D^{s}, $\sigma^{\mathrm{s}}_{\mathrm{eff}}$, k_0, and $c^{\mathrm{s}}_{\mathrm{max}}$ with their tilde-marked counterparts from Eq. 5.

Numerical Experiments

We conduct a series of numerical experiments to investigate the ability of the three P2D models (DFN, mDFN, and SPM) with the two alternative (AE and AM) parameterizations to accurately predict the lithiation curves for LMBs. These curves describe the temporal evolution of cell terminal voltage $U_{\mathrm{cell}} = \phi_{\mathrm{s}}(L, t) - \phi_{\mathrm{s}}(0, t)$, where the reference potential $\phi_{\mathrm{s}}(0, t)$ is set to 0 and the solid-phase potential $\phi_{\mathrm{s}}(x, t)$ for any $x > 0$, including $x = L$, is computed by solving Eqs. 1–3.

Although our approach is general and applicable to any Li-ion or Li-metal battery, we demonstrate it on a LMB with nickel manganese cobalt oxides cathode (NMC622), carbon additives and polyvinylidene fluoride binder, and $LiPF_6$ electrolyte.[12] The electrochemical properties of this reference LMB[12,16] are summarized in Table I. For these parameters, all three P2D models, i.e., Eqs. 1–3, are solved using the open source software package Python Battery Mathematical Modelling (PyBaMM);[28] the software routines were modified to accommodate time- and radius-dependent parameters; each subdomain (separator, porous electrode and particle) is discretized with 40 elements. In the mDFN model, the active particles are assigned a lognormal distribution with the mean and standard deviation from Ref. 12.

The three P2D models (DFN, mDFN, and SPM) with the two alternative (AE and AM) parameterizations yield six alternative methods for computing the lithiation curves; they are labeled Methods 1 through 6 in Table II. The AE parameterization can either use the standard/unmodified value of the Bruggeman exponent $b^{\mathrm{e}} = 1.5$ or to estimate this value by solving the closure problem, Eq. 4; the latter approach yields $b^{\mathrm{e}} = 2.67$, as reported in Table III and referred to below as the AE+ parameterization. This closure problem is solved with the open source software package Fipy[29] on the REV in Fig. 1. The radius of the spherical particles forming the REV is selected to match the experimentally measured porosity ω, and the pore space Ω is discretized into 349522 elements using the open source software package GMSH.[30]

The AM parameterization uses the volume fraction of active material in the solid phase, v, and the transport properties of its two components (active material and CBD) as inputs to calculate the effective properties of the single homogenized solid phase (Table III). The value of v is computed for the FCC periodic microstructure of the porous electrode (Fig. 1). While the

Table II. The three P2D models (DFN, mDFN, and SPM) with the two alternative (AE and AM) parameterizations are denoted by Method 1–Method 6. The enhanced versions of these parameterizations are denoted by the plus sign.

	DFN	mDFN	SPM
AE parameterization	Method 1	Method 3	Method 5
AE+ parameterization	Method 1+	Method 3+	Method 5+
AM parameterization	Method 2	Method 4	Method 6
AM+ parameterization	Method 2+	Method 4+	–

Table III. Modified (effective) values of the physicochemical properties from Table I resulting from the AE+ and AM parameterizations of the P2D models. The only difference between the AE and AE+ parameterizations is that the former leaves the Bruggeman exponent unchanged, $b^e = 1.5$.

	AE+	AM
Porosity, ω (ε for AE)	0.417	0.305
Solid-phase volume fraction, $1-\omega$ ($1-\varepsilon$ for AE)	0.583	0.695
Volume ratio of active particle in solid phase, v	1	0.839
Solid-particle radius, R^s ($\tilde{R}^s$) [μm]	7.84	8.31
Solid-phase diffusivity, D^s ($\tilde{D}^s$) [m^2/s]	$4.303 \cdot 10^{-14}$	$1.954 \cdot 10^{-14}$
Solid-phase conductivity, σ^s ($\tilde{\sigma}^s$) [S/m]	2.8	0.364
Reaction rate, k_0 ($\tilde{k}_0$) [m$^{2.5}$/s/mol$^{0.5}$]	$1.523 \cdot 10^{-11}$	$0.772 \cdot 10^{-11}$
Maximum Li concentration, c^s_{max} ($\tilde{c}^s_{max}$) [mol/m^3]	50 451	42 328
Cathode Bruggeman exponent b^e	2.67	1.5
Cathode Bruggeman exponent b^s	1.5	1.5

representative active material radius R^s is kept unchanged, the CBD coating thickness d_{CBD} and, hence, the radius of the homogenized particle, $\tilde{R}^s$, are computed to obtain the measured solid phase volume fraction. The same effective parameters are retained also when considering a distribution of particles in the mDFN model.

For reasons described in the Introduction, the lithiation curves obtained via pore-scale simulations[12] serve as the ground truth that provide a baseline for the assessment of the accuracy of the alternative parameterizations of the P2D models in Table II. These simulations consist of numerical solution of the three-dimensional mass and charge balance Eqs. for the electrolyte-filled pore space and the ambient active material; an interfacial kinetics model couples these PDEs at the liquid-solid interfaces. The simulations[12] are carried out for a hybrid porous microstructure, in which a tomographically accurate active material geometry is enhanced by a synthetically generated CBD phase with assigned volume fraction. Our P2D simulations and their pore-scale counterparts are carried out for the same porosity, ω, and active-material volume fraction, $1-\varepsilon$; no fitting parameters are used to improve the match between the P2D and pore-scale predictions of the lithiation curves.[d]

Results and Discussion

We use a series of numerical experiments to identify a Method, which yields the most accurate approximation of the pore-scale estimate of the lithiation curves for the LMB characterized by the parameter values in Table I. In another set of numerical experiments, we use this Method as a predictive tool to quantify the impact of modifying CBD properties (the volume fraction and composition in Table IV) on the overall cell performance.

Method verification.—Figure 2 compares predictions of the lithiation curves obtained via the DFN model with the alternative parameterizations from Table II, for several values of the discharge current density i_{dis}. Also shown in this figure are the lithiation curves computed via the pore-scale simulations,[12] which serve as the ground truth. Figure 2 reveals that the standard DFN parameterization (Method 1) fails to account for the CBD presence, whose impact increases with i_{dis}, consistently over-predicting the LMB capacity. Both Method 1+ and Method 2 improve the prediction accuracy at all tested discharge currents, with Method 1+ adequately representing the lithiation curves throughout the discharge process. Method 2 accurately captures the final discharge time for all i_{dis}, but over-estimates the voltage drop at early times. That is because the AM parameterization in Eq. 5 ignores the pre-asymptotic time-dependence of the effective coefficients, whose persistence increases with discharge current; the time-to-asymptote is directly related to the intercalation delay time t_{del} induced by the CBD phase, which increases with i_{dis} (Fig. 2). When choosing between Method 1+ and Method 2 it is worthwhile recognizing that Method 1+ requires the solution of a closure problem on a representative microstructure of the porous electrode, while Method 2 utilizes the effective coefficients that can be readily computed from the active material volume fraction in the solid phase v and phase-specific transport properties.

Regardless of its parameterization (Methods 5 and 6), the SPM model yields predictions of the lithiation curves that are significantly less accurate than those obtained via the corresponding DFN model (Methods 1 and 2), especially at higher C-rates (Fig. 3). The AE parameterizations of the SPM (Methods 5 and 5+) are insensitive to the increased tortuosity caused by the CBD presence, since the assumption of the spatially uniform Li^+ concentration c^e is blind to any changes in the effective diffusion coefficient in the electrolyte phase, D_{eff}^e. This approximation becomes progressively less accurate as the discharge current density i_{dis} (C-rate) increases, i.e., when

[d] In lieu of performing pore-scale simulations, we use their output reported in Fig. SI-1c from Supporting Information in Ref. 12. This output is in the form of lithiation curves for four discharge scenarios with increasing current density and corresponds to "Microstructure B". The latter consists of CBD-coated active particles and shares the same electrode thickness as the one utilized in our P2D simulations. In Fig. SI-1c, the terminal voltage U_{cell} is exhibited as function of transferred charge $\mathcal{C} = i_{dis}t$ [mAh/cm^2]; to plot U_{cell} as function of time t, we divide transferred charge by the current density i_{dis} corresponding to each C-rate scenario, i.e., $t = \mathcal{C}/i_{dis}$.

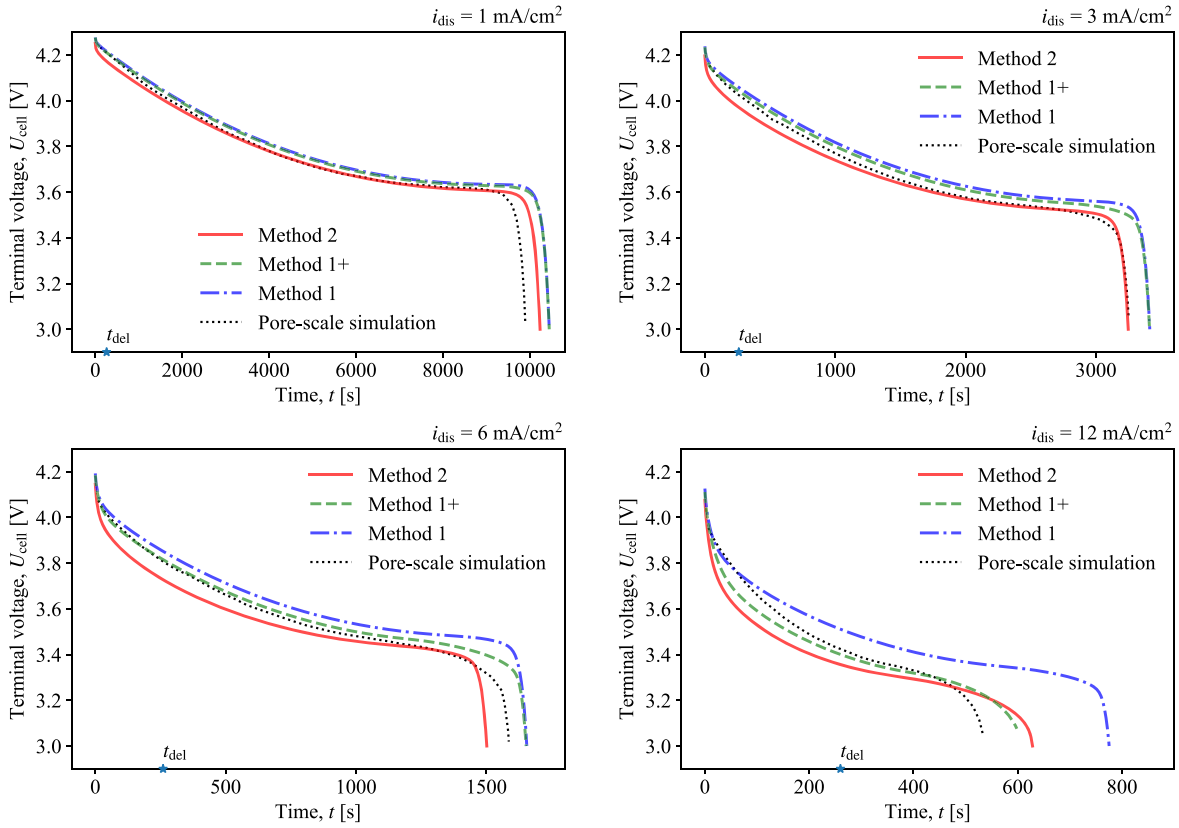

Figure 2. Lithiation curves predicted by the DFN model with the alternative parameterizations from Table II, for different discharge current densities i_{dis}. Also shown in this figure are the lithiation curves computed via the pore-scale simulations,[12] which serve as the ground truth. The star indicates the intercalation time-delay t_{del}. The parameter values used in these simulations are listed in Tables I and III.

Table IV. Values of the effective parameters in Method 2.

	CBD volume fraction, $1-v$			
	0	0.06	0.10	0.14
Porosity, ω [−]	0.417	0.357	0.317	0.277
Solid phase volume fraction, $1-\omega$ [−]	0.583	0.643	0.683	0.723
Solid particle reference radius, $\tilde{R}^s$ [μm]	7.84	8.1	8.27	8.42
Coefficient of variation, $\sigma_R/\tilde{R}^s$ [−]	0.46	0.46	0.46	0.46
Solid-phase diffusivity, $\tilde{D}^s$ [10^{-14} m^2/s]	4.303	3.158	2.177	1.549
Solid-phase conductivity, $\tilde{\sigma}^s$ [S/m]	2.8	0.596	0.398	0.302
Reaction rate, $\tilde{k}_0$ [10^{-11} m$^{2.5}$/s/mol$^{0.5}$]	1.523	0.818	0.781	0.751
Maximum Li concentration, $\tilde{c}^s_{max}$ [mol/m^3]	50 451	45 759	43 085	40 663

the availability of Li^+ in the electrolyte plays a limiting role in the cell performance. On the other hand, the AM parameterizations (Methods 6 and 6+) are tailor-made for the SPM, since they capture the CBD-induced changes in the active material properties. Method 6 yields accurate predictions of the total discharge time for all discharge rates and, relative to Method 1, suffers less from the constant coefficients parameterization (Eq. 5) at early times.

The lithiation curves predicted via the mDFN model with the alternative parameterization strategies (Methods 3 and 4 from Table II) are exhibited in Fig. 4. The computation of the Bruggeman exponent b^e in Method 4+ is computationally demanding, since it involves the solution of the closure problem, Eq. 4, for each realization of the particle radius drawn from a given distribution; consequently, we do not implement it here. The AM parameterization (Method 4) has the biggest impact on the predictions of the voltage drop at early times, especially for intermediate discharge currents. We posit that this is due to transport within large particles (tail of the distribution), whose intercalation delay time t_{del} is of the same order of magnitude as the discharge time. To confirm this hypothesis, we repeated the simulations (not shown here) for a smaller standard deviation of particle sizes and observed an improved agreement between the mDFN and pore-scale simulations. Overall, the mDFN model does not significantly improve the prediction accuracy of the lithiation curves in the presence of CBD, while increasing the computational time by more than one order of magnitude relative to the DFN model.

The AM parameterization, Eq. 5, employs the asymptotic value of the semi-analytical function $\tilde{D}^s(t)$; this asymptote is strictly valid for $t > t_{del}$ and is used for convenience.[25] To explore the impact of this procedure, we plot the lithiation curves computed via the DFN (Fig. 5) and mDFN (Fig. 6) models with the AM+ parameterization (Method 2+ and Method 4+ from Table II, respectively). Method 2 + provides more accurate predictions of the LBM discharge at early times than Method 2 does, while displaying enhanced sharpness of

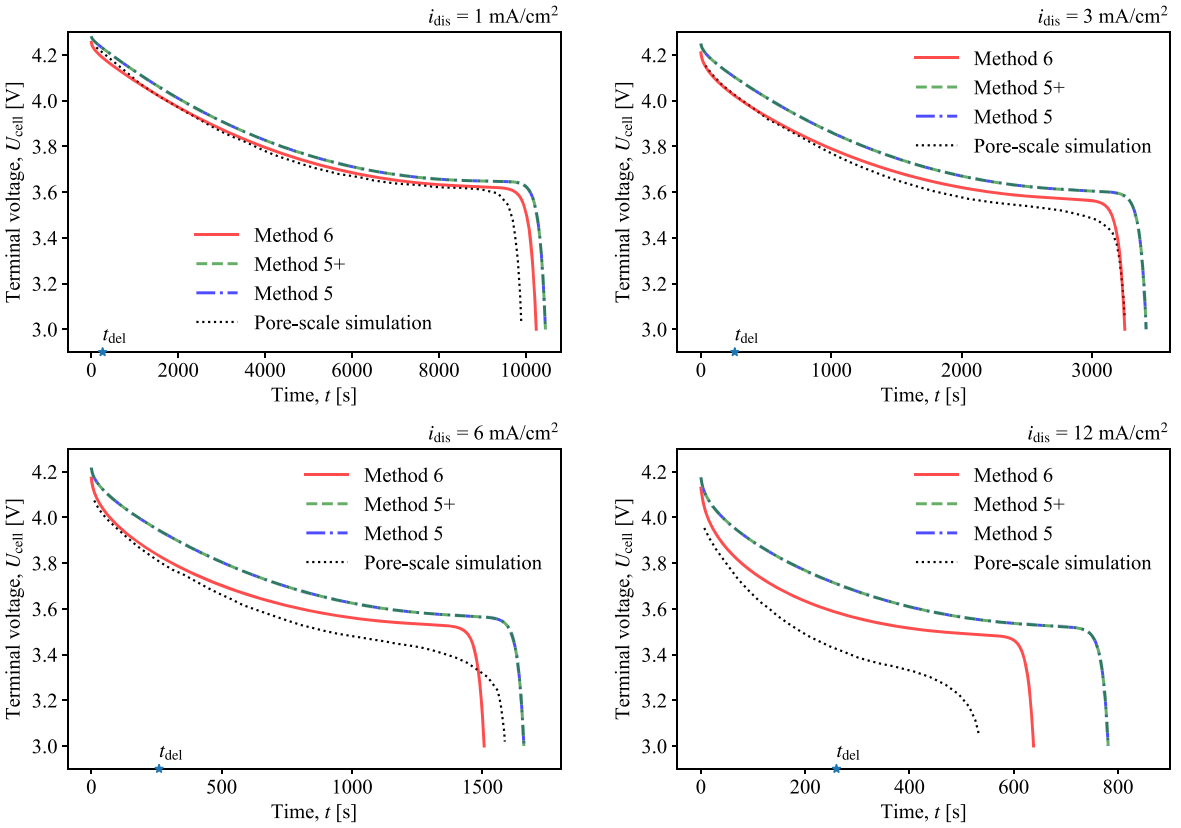

Figure 3. Lithiation curves predicted by the SPM model with the alternative parameterizations from Table II, for different discharge current densities i_{dis}. Also shown in this figure are the lithiation curves computed via the pore-scale simulations,[12] which serve as the ground truth. The star indicates the intercalation time-delay t_{del}. The parameter values used in these simulations are listed in Tables I and III.

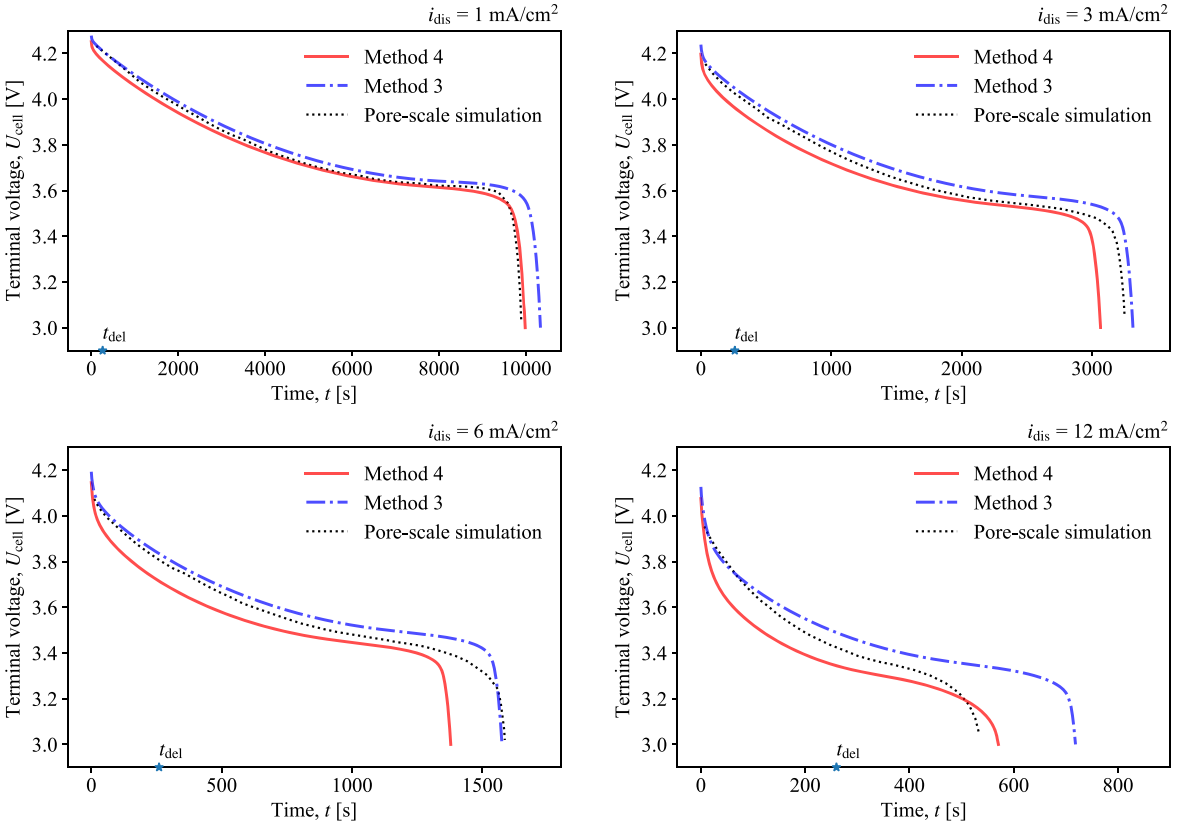

Figure 4. Lithiation curves predicted by the mDFN model with the alternative parameterizations from Table II, for different discharge current densities i_{dis}. Also shown in this figure are the lithiation curves computed via the pore-scale simulations,[12] which serve as the ground truth. The star indicates the intercalation time-delay t_{del}. The parameter values used in these simulations are listed in Tables I and III.

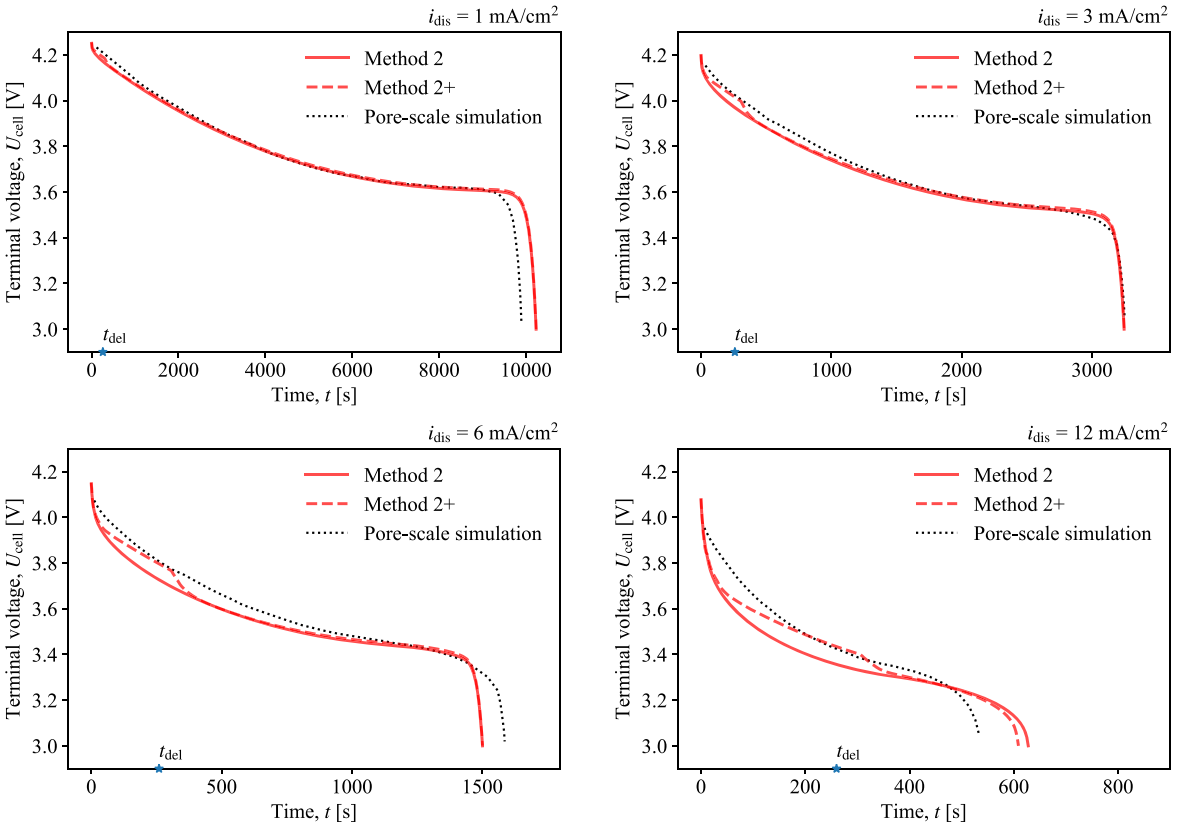

Figure 5. Lithiation curves predicted by the DFN model with the AM and AM+ parameterizations (Method 2 and Method 2+ from Table II, corresponding to the constant and time-varying $\tilde{D}^s$, respectively) for different discharge current densities i_{dis}. Also shown in this figure are the lithiation curves computed via the pore-scale simulations,[12] which serve as the ground truth. The star indicates the intercalation time-delay τ_{del}. The parameter values used in these simulations are listed in Tables I and III.

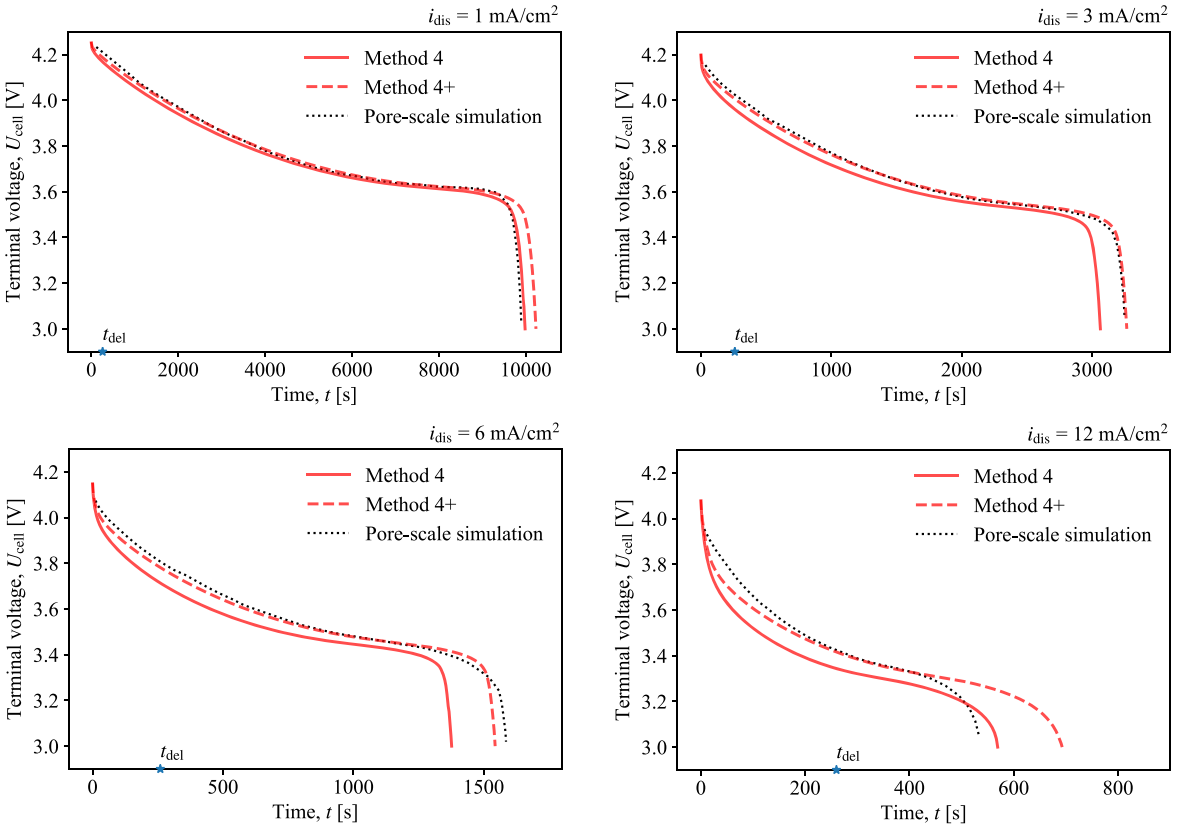

Figure 6. Lithiation curves predicted by the mDFN model with the AM and AM+ parameterizations (Method 4 and Method 4+ from Table II, corresponding to the constant and time-varying $\tilde{D}^s$, respectively) for different discharge current densities i_{dis}. Also shown in this figure are the lithiation curves computed via the pore-scale simulations,[12] which serve as the ground truth. The star indicates the intercalation time-delay τ_{del}. The parameter values used in these simulations are listed in Tables I and III.

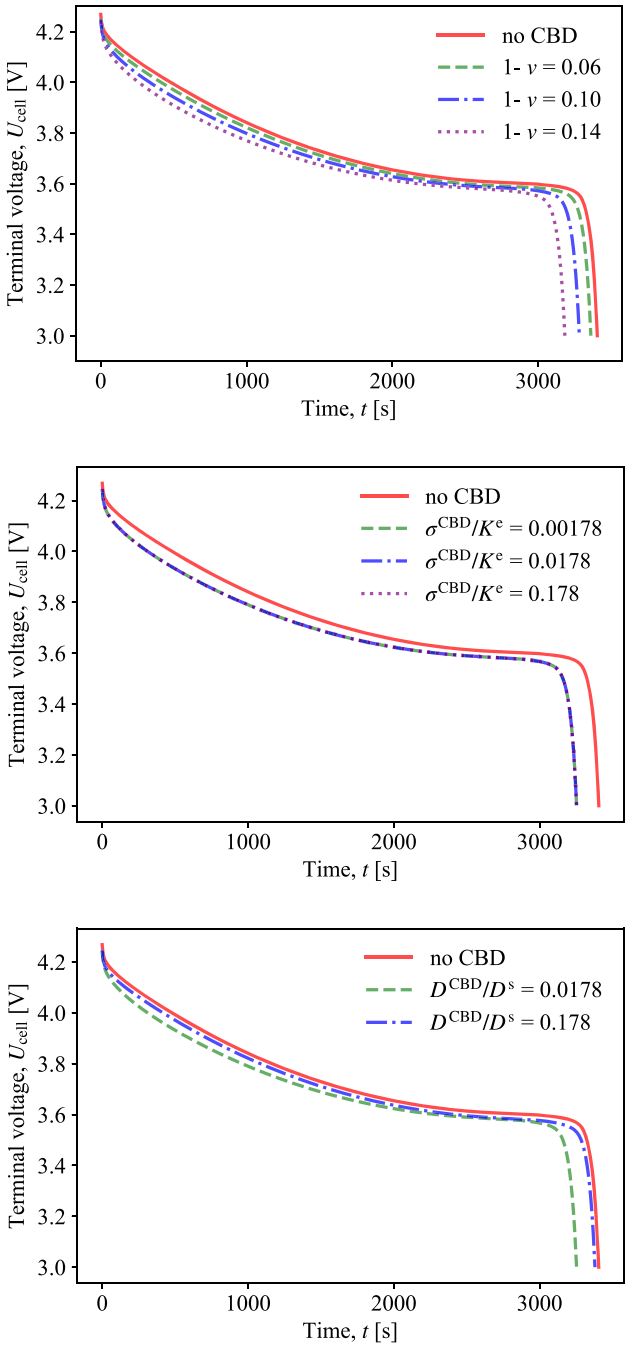

Figure 7. Lithiation curves for LMBs, whose porous cathode employs different CBD configurations. Each of these configurations differs from the reference LBM properties in Table III by a single CBD characteristic: the CBD volume fraction $1 - v$ (top), the CBD ionic conductivity σ^{CBD} (middle), and the CBD ionic diffusivity D^{CBD} (bottom). The corresponding model parameters are collated in Table IV. The discharge current density is set to $i_{dis} = 3$ mA/cm^2.

the voltage profile at the intercalation delay time t_{del}. The improvement is even more noticeable when Method 4+ is used instead of Method 4. The increased accuracy of Methods 2+ and 4+ comes at the cost of the increased complexity in computing the time-varying effective diffusivity $\tilde{D}^s(t)$ and the necessity to modify a P2D simulator to allow for time-dependent parameterizations. We argue that Method 2 provides an attractive balance between the computational complexity and the prediction accuracy.

Impact of CBD properties on cell performance.—Having established the ability of the properly parameterized DFN and mDFN models to accurately capture the impact of CBD on the lithiation curves for the previously studied LMB,[12] we proceed to use these models to forecast the performance of a cell utilizing different volume fractions and material properties of CBD. The effective parameters for Method 2, computed via Eq. 5, are summarized in Table IV.

Figure 7 exhibits the lithiation curves for several CBD configurations predicted via Method 2. Each of these configurations differs from the reference LBM properties in Table III by a single CBD characteristic: the CBD volume fraction in the solid phase $1 - v$ (Fig. 7a), the CBD ionic conductivity σ^{CBD} (Fig. 7b), and the CBD ionic diffusivity D^{CBD} (Fig. 7c). The battery discharge time decreases as either the CBD volume fraction increases or the CBD ionic diffusivity decreases, and is insensitive to the ionic conductivity of CBD. The quantitative nature of these observations can be used in the optimal design of porous cathodes.

Conclusions

P2D models are routinely used to predict the lithiation curves for energy storage devices, including LMBs. The performance of such models is as good as their parameterization, which remains a challenge especially in the presence of CBD. We proposed two alternative parameterization strategies, which explicitly account for the CBD volume fraction and physical properties. The first (electrolyte-augmented parameterization or AE+) aggregates CBD with the electrolyte-filled pore space and expresses the augmented Bruggeman exponent in terms of a solution of microstructure-specific closure problem. The second (active material-augmented parameterization or AM) treats CBD and active particles as a composite solid phase, whose effective properties are computed (semi-)analytically via homogenization. When applied to the three P2D models (DFN, mDFN, and SPM), these parameterizations, and their enhancements, give rise to Methods 1–6, whose labels are assigned in Table II. We conducted a series of numerical experiments that lead to the following major conclusions.

- Both AE+ and AM parameterizations of the three P2D models outperform their currently used counterparts in terms of the prediction accuracy of the lithiation curves at all C-rates considered.
- Regardless of its parameterization (Methods 5 and 6), the SPM model yields predictions of the lithiation curves that are significantly less accurate than those obtained via the corresponding DFN model (Methods 1 and 2), especially at higher C-rates.
- The mDFN model provides a modest improvement in the prediction accuracy of the lithiation curves in the presence of CBD, while increasing the computational time by more than one order of magnitude relative to the DFN model.
- Increased accuracy of the transient parameterizations is balanced by the cost of computing the time-varying effective diffusivity and the need to modify a P2D simulator. Our AM parameterization of the DFN model provides an attractive middle ground between the model complexity and the prediction accuracy.
- The battery discharge time decreases as either the CBD volume fraction increases or the CBD ionic diffusivity decreases, and is insensitive to the CBD ionic conductivity. The quantitative nature of these observations can be used in the optimal design of porous cathodes.

The accuracy of the alternative P2D Methods discussed above is ascertained in terms of their ability to match the lithiation curves predicted via the pore-scale simulations[12] for a given LMB microstructure. While we treat these pore-scale results as ground truth, it is worthwhile mentioning that they depart from experimental data[12] at high C-rates. This suggests the need to construct more representative, yet computationally tractable, alternatives to the currently used

P2D models. Other venues for future research are to study CBD morphologies other than a uniform CBD coating of spherical active-material particles, and Li batteries other than NMC622 used here for demonstration purposes.

Acknowledgments

This work was supported in part by Hyundai Motor Group and by Air Force Office of Scientific Research under award number FA9550-21-1-0381.

ORCID

Weiyu Li https://orcid.org/0000-0002-7857-8115
Daniel M. Tartakovsky https://orcid.org/0000-0001-9019-8935

References

1. Y. Wu, E. Rahm, and R. Holze, "Carbon anode materials for lithium ion batteries." *Journal of Power Sources*, **114**, 228 (2003).
2. X.-B. Cheng, R. Zhang, C.-Z. Zhao, and Q. Zhang, "Toward safe lithium metal anode in rechargeable batteries: A review." *Chem. Rev.*, **117**, 10403 (2017).
3. X. Zhang and D. M. Tartakovsky, "Optimal design of nanoporous materials for electrochemical devices." *Appl. Phys. Lett.*, **110**, 143103 (2017).
4. W. Li, H. A. Tchelepi, Y. Ju, and D. M. Tartakovsky, "Stability-guided strategies to mitigate dendritic growth in lithium-metal batteries." *J. Electrochem. Soc.*, **169**, 060536 (2022).
5. H. Zheng, R. Yang, G. Liu, X. Song, and V. S. Battaglia, "Cooperation between active material, polymeric binder and conductive carbon additive in lithium ion battery cathode." *The Journal of Physical Chemistry C*, **116**, 4875 (2012).
6. M. Indrikova, S. Grunwald, F. Golks, A. Netz, B. Westphal, and A. Kwade, "The morphology of battery electrodes with the focus of the conductive additives paths." *J. Electrochem. Soc.*, **162**, A2021 (2015).
7. A. Manthiram, "A reflection on lithium-ion battery cathode chemistry." *Nat. Commun.*, **11**, 1 (2020).
8. D. E. Stephenson, B. C. Walker, C. B. Skelton, E. P. Gorzkowski, D. J. Rowenhorst, and D. R. Wheeler, "Modeling 3D Microstructure and Ion Transport in Porous Li-Ion Battery Electrodes." *J. Electrochem. Soc.*, **158**, 781 (2011).
9. N. A. Zacharias, D. R. Nevers, C. Skelton, K. Knackstedt, D. E. Stephenson, and D. R. Wheeler, "Direct measurements of effective ionic transport in porous li-ion electrodes." *J. Electrochem. Soc.*, **160**, A306 (2013).
10. A. Mistry, S. Trask, A. Dunlop, G. Jeka, B. Polzin, P. P. Mukherjee, and V. Srinivasan, "Quantifying negative effects of carbon-binder networks from electrochemical performance of porous li-ion electrodes." *J. Electrochem. Soc.*, **168**, 070536 (2021).
11. M. Stein, A. Mistry, and P. P. Mukherjee, "Mechanistic understanding of the role of evaporation in electrode processing." *J. Electrochem. Soc.*, **164**, A1616 (2017).
12. S. Hein, T. Danner, D. Westhoff, B. Prifling, R. Scurtu, L. Kremer, A. Hoffmann, A. Hilger, M. Osenberg, and I. Manke, "Influence of conductive additives and binder on the impedance of lithium-ion battery electrodes: Effect of morphology." *J. Electrochem. Soc.*, **167**, 013546 (2020).
13. S. R. Daemi, C. Tan, T. Volkenandt, S. J. Cooper, A. Palacios-Padros, J. Cookson, D. J. Brett, and P. R. Shearing, "Visualizing the carbon binder phase of battery electrodes in three dimensions." *Materials*, **1**, 3702 (2018).
14. L. Zielke, T. Hutzenlaub, D. R. Wheeler, I. Manke, T. Arlt, N. Paust, R. Zengerle, and S. Thiele, "A combination of x-ray tomography and carbon binder modeling: reconstructing the three phases of LiCoO2 Li-ion battery cathodes." *Adv. Energy Mater.*, **4**, 1301617 (2014).
15. A. N. Mistry, K. Smith, and P. P. Mukherjee, "Secondary-phase stochastics in lithium-ion battery electrodes." *ACS Applied Materials & Interfaces*, **10**, 6317 (2018).
16. L. S. Kremer, A. Hoffmann, T. Danner, S. Hein, B. Prifling, D. Westhoff, C. Dreer, A. Latz, V. Schmidt, and M. Wohlfahrt-Mehrens, "Manufacturing process for improved ultra-thick cathodes in high-energy lithium-ion batteries." *Energy Technology*, **8**, 1900167 (2020).
17. B. Trembacki, E. Duoss, G. Oxberry, M. Stadermann, and J. Murthy, "Mesoscale electrochemical performance simulation of 3d interpenetrating lithium-ion battery electrodes." *J. Electrochem. Soc.*, **166**, A923 (2019).
18. X. Zhang and D. M. Tartakovsky, "Effective ion diffusion in charged nanoporous materials." *J. Electrochem. Soc.*, **164**, E53 (2017).
19. D. M. Tartakovsky and M. Dentz, "Diffusion in porous media: phenomena and mechanisms." *Transport in Porous Media*, **130**, 105 (2019).
20. M. Doyle, T. F. Fuller, and J. Newman, "Modeling of galvanostatic charge and discharge of the lithium/polymer/insertion cell." *J. Electrochem. Soc.*, **140**, 1526 (1993).
21. T. L. Kirk, C. P. Please, and S. J. Chapman, "Physical modelling of the slow voltage relaxation phenomenon in lithium-ion batteries." *J. Electrochem. Soc.*, **168**, 060554 (2021).
22. A. Jokar, B. Rajabloo, M. Désilets, and M. Lacroix, "Review of simplified Pseudo-two-Dimensional models of lithium-ion batteries." *Journal of Power Sources*, **327**, 44 (2016).
23. F. L. Usseglio-Viretta, A. Colclasure, A. N. Mistry, K. P. Y. Claver, F. Pouraghajan, D. P. Finegan, T. M. M. Heenan, D. Abraham, P. P. Mukherjee, and D. Wheeler, "Resolving the discrepancy in tortuosity factor estimation for Li-ion battery electrodes through micro-macro modeling and experiment." *J. Electrochem. Soc.*, **165**, A3403 (2018).
24. S. J. Cooper, A. Bertei, P. R. Shearing, J. Kilner, and N. P. Brandon, "TauFactor: An open-source application for calculating tortuosity factors from tomographic data." *SoftwareX*, **5**, 203 (2016).
25. W. Li and D. M. Tartakovsky, "Effective representation of active material and carbon binder in porous electrodes." *J. Electrochem. Soc.*, **169**, 040556 (2022).
26. S. G. Marquis, V. Sulzer, R. Timms, C. P. Please, and S. J. Chapman, "An asymptotic derivation of a single particle model with electrolyte." *J. Electrochem. Soc.*, **166**, A3693 (2019).
27. G. L. Plett, *Battery Management Systems, vol 1: Battery Modeling* (Artech House, Boston, MA) (2015).
28. V. Sulzer, S. G. Marquis, R. Timms, M. Robinson, and S. J. Chapman, "Python battery mathematical modelling (PyBaMM)." *Journal of Open Research Software*, **9**, 14 (2021).
29. J. E. Guyer, D. Wheeler, and J. A. Warren, "FiPy: partial differential equations with python." *Computing in Science & Engineering*, **11**, 6 (2009).
30. C. Geuzaine and J.-F. Remacle, "Gmsh: A 3-D finite element mesh generator with built-in pre-and post-processing facilities." *International Journal for Numerical Methods in Engineering*, **79**, 1309 (2009).